Obrabotka metallov (tekhnologiya, oborudovanie, instrumenty) = Metal Working and Material Science. 2025 vol. 27 no. 4 pp. 62–79
ISSN: 1994-6309 (print) / 2541-819X (online)
DOI: 10.17212/1994-6309-2025-27.4-62-79

NSTU NETI

Obrabotka metallov - Metal Working and Material Science

Journal homepage: http://journals.nstu.ru/obrabotka_metallov

Milling of a blank from austenitic stainless steel AISI 321, deposited using wire-arc additive manufacturing (WAAM)

Qingrong Zhang [1, c], ***Vasiliy Klimenov*** [1, b, *], ***Viktor Kozlov*** [1, c], ***Dmitry Chinakhov*** [2, d], ***Zeli Han*** [1, e], ***Mengxu Qi*** [1, f], ***Zeru Ding*** [1, g], ***Menghua Pan*** [1, h]

[1] National Research Tomsk Polytechnic University, 30 Lenin Avenue, Tomsk, 634050, Russian Federation
[2] Novosibirsk State Technical University, 20 Prospekt K. Marksa, Novosibirsk, 630073, Russian Federation

[a] https://orcid.org/0009-0002-7820-1227, cinzhun1@tpu.ru; [b] https://orcid.org/0000-0001-7583-0170, klimenov@tpu.ru;
[c] https://orcid.org/0000-0001-9351-5713, kozlov-viktor@bk.ru; [d] https://orcid.org/0000-0002-4319-7945, chinakhov@corp.nstu.ru;
[e] https://orcid.org/0000-0001-6502-6541, hanzelizy@gmail.com; [f] https://orcid.org/0000-0003-3738-0193, mensyuy1@tpu.ru;
[g] https://orcid.org/0009-0009-6303-7453, czezhu1@tpu.ru; [h] https://orcid.org/0009-0004-1128-9935, menhua1@tpu.ru

ARTICLE INFO

Article history:
Received: 28 May 2025
Revised: 18 June 2025
Accepted: 06 October 2025
Available online: 15 December 2025

Keywords:
Wire-arc additive manufacturing
Cold metal transfer
Austenitic stainless steel ER321
Microstructure
Mechanical property
Milling force
Roughness

Acknowledgements
The equipment used for the research was provided by the Shared Use Center "Structure, Mechanical and Physical Properties of Materials" at Novosibirsk State Technical University.

ABSTRACT

Introduction. Wire arc additive manufacturing (*WAAM*), due to its "design as manufacturing" characteristic, is gradually becoming one of the most promising technologies. However, at present, there are no comprehensive comparative studies on the microstructure and mechanical properties of deposited samples made from austenitic stainless steel at different locations of the sample. In addition, their machinability remains insufficiently investigated. **The purpose of this study** is to compare the microstructure and mechanical properties of samples made of austenitic stainless steel *ER321* (analogues – *AISI 321*, 0.08% *C*-18% *Cr*-10% *Ni-Ti*) obtained by the *WAAM* method at different locations within the sample and to assess their machinability by the magnitude of the components of the cutting force during end milling and the roughness of the machined surface. The properties and microstructure of samples obtained by wire-arc additive technology are investigated, and milling forces **are investigated**. The effect of the feed on the components of the cutting force and the roughness of the machined surfaces during conventional milling of *ER321* steel workpieces using 12 mm diameter cemented carbide end mills with a wear-resistant *AlTiN* coating applied by physical vapor deposition (*PVD*) is determined. **Research methods.** The content of elements and the solidification pattern in various parts of the workpieces were determined using X-ray microanalysis. The microstructure of the samples was studied by a metallographic method. Stress-strain diagrams were obtained by tensile tests, and the microhardness of the samples was also measured. In comparison with the pattern of conventional milling of rolled workpieces, a pattern of changes in cutting forces and surface roughness was established depending on the feed rate during milling of deposited workpieces. **Results and discussion.** During deposition, ferrite with a vermicular morphology is primarily formed in the lower region of the sample, whereas austenite with a dendritic ferrite structure is observed in other regions. The microhardness values of the deposited and rolled samples are close, averaging around 230 HV0.1. The ultimate tensile strength of the rolled samples is 666 MPa, which is approximately 40 MPa higher than that of the deposited samples. During milling of the deposited workpieces, the lateral cutting force acting perpendicular to the feed direction is greater, and the surface quality is poorer. During milling of deposited workpieces, the lateral cutting force acting perpendicular to the feed direction is greater, and the surface quality is poorer. During milling of deposited workpieces, the feed force acting in the feed direction is greater under high feed rates.

For citation: Zhang Q., Klimenov V.A., Kozlov V.N., Chinakhov D.A., Han Z., Qi M., Ding Z., Pan M. Milling of a blank from austenitic stainless steel AISI 321, deposited using wire-arc additive manufacturing (WAAM). *Obrabotka metallov (tekhnologiya, oborudovanie, instrumenty) = Metal Working and Material Science*, 2025, vol. 27, no. 4, pp. 62–79. DOI: 10.17212/1994-6309-2025-27.4-62-79. (In Russian).

*** Corresponding author**
Klimenov Vasiliy A., D.Sc. (Engineering), Professor
National Research Tomsk Polytechnic University,
30 Lenin Avenue,
634050, Tomsk, Russian Federation
Tel.: +7 913 850-44-51, **e-mail:** klimenov@tpu.ru

Introduction

Wire arc additive manufacturing (*WAAM*) offers high deposition rates (up to 800 g/min), low production costs (approximately an order of magnitude lower than powder-based additive methods), and significant advantages for the 3D prototyping of complex structures and the on-demand fabrication of functional materials. These benefits position *WAAM* as a leading direction in the development of additive manufacturing (*AM*) [1–7]. Among welding techniques, cold metal transfer (*CMT*) is particularly notable due to its controlled short-circuiting process. This method significantly reduces heat input, promotes grain refinement, and is widely used in *WAAM* when dimensional accuracy and surface roughness requirements are moderate [6, 7].

Austenitic stainless steel, valued for its high ductility, excellent strength, and good corrosion resistance, has become a primary material for additive manufacturing in engineering and medical applications [8]. However, the complexity of *AM* thermal cycles complicates the prediction of microstructure and mechanical properties in fabricated parts. For instance, *AISI 308LSi* stainless steel specimens produced by electric-arc deposition using graphite sliders in an argon atmosphere exhibit more uniform structural growth and an average 12% increase in hardness due to a more intensive δ-ferrite to austenite transformation [9]. Variations in cooling conditions can lead to a 10% difference in ultimate tensile strength between the upper and lower sections of *AISI 304* stainless steel specimens [10]. Similarly, a direct heat transfer in *AISI 316L* steel results in a 10% anisotropy in tensile strength [11].

Furthermore, the surface quality of *AM*-produced parts, particularly those made by *WAAM*, is often low. High heat input causes instability and spreading of the weld pool, accompanied by spatter adhesion to the specimen surface. According to [12], the lateral surface roughness of *WAAM* products, defined by weld bead geometry, can reach 1.06 mm. Consequently, mechanical post-processing is typically required to improve surface finish [13]. The machining of stainless steel is complicated by its high ductility, which promotes significant work hardening, chip adhesion to the tool, built-up edge formation, and micro-voids on the machined surface. While *Dabwan* et al. [14] investigated cutting forces and surface quality in additively manufactured *316L* stainless steel under different printing parameters, and *Guo* et al. [15] studied these parameters for high-power direct laser deposition at various milling rates, neither study compared additively manufactured specimens with conventionally rolled counterparts. Given the prevalent use of wire from the People's Republic of China (*PRC*) in wire-feed electron beam additive manufacturing, it is crucial to compare products fabricated in Russia and the *PRC*, considering differences in synthesis processes and the chemical composition of the feedstock wire.

Current research predominantly focuses on the machinability of refractory nickel and titanium alloys produced by *AM*, while the machinability of austenitic stainless steels remains largely unexplored [16]. Therefore, investigating the machinability of austenitic stainless steel specimens, especially those fabricated by *WAAM*, and comparing them with rolled specimens is necessary.

The purpose of this work is to determine the microstructure and mechanical properties of a *WAAM*-fabricated specimen in different regions and to compare its machinability with that of a rolled specimen. The following investigations were conducted:

– Determination of the solidification mechanism based on the chemical composition in different regions of the *WAAM*-fabricated specimen.

– Analysis of the relationship between mechanical properties (hardness, ultimate tensile strength, ultimate elongation) and microstructure in different regions of the fabricated specimen.

– Comparison of changes in cutting forces and surface roughness as a function of feed rate during the milling of *WAAM*-fabricated and rolled specimens.

Notation

λ – thermal conductivity, W/(m·ºC)
C – heat capacity, J/(kg·K)
γ – austenite

δ – ferrite
L – liquid
γ_{cut} – face angle of a cutter, deg.
α_{cut} – back angle of a cutter, deg.
z – number of teeth of a cutter, pcs.
B – milling width, mm
t – milling depth, mm
s_m – feed rate, mm/min
s_t – feed per tooth, mm/min
n – rotational speed of a cutter, rpm
v – cutter speed, mm/min
ψ – engagement angle, deg. It indicates the angular location of the cutting edge of the cutter tooth tip from the pierce point to its location at opposed milling
$P_h(F_x)$ – feed force, N. It is oriented along the feed per minute direction. In opposed milling, the feed force is directed to the specimen in the opposite direction of the feed per minute. In cutdown milling, this force is directed to the specimen and coincides with the direction of the feed per minute
$P_v(F_y)$ – lateral force, N. It is directed normal to the direction of the feed per minute
$P_x(F_z)$ – axial force, N. It is directed along the cutter axis
P_y – radial force, N. It is directed normal to the cutter speed vector and from the axis of rotation to the point considered on the cutting edge
P_z – tangential force, N. This force coincides with the direction of the cutter speed vector
N – normal force. This force is directed from the cut surface to the back surface of the cutting edge
P_{hv} – total force P_h and P_v, N. $P_{hv} = (P_h^2 + P_v^2)^{1/2}$
P_{yz} – total force P_y and P_z, N. $P_{yzv} = (P_y^2 + P_z^2)^{1/2}$
T – temperature, °C
R_a – surface roughness, μm. It means arithmetic mean from absolute values of the surface profile deviation within the specimen length
P_{tot} – total milling force, N. $P_{tot} = (Ph^2+Pv^2+Px^2)^{1/2}$
h_p – height of protrusion not removed by a cutter, μm

Methods

A specimen measuring 194×80×34 mm was fabricated using *WAAM* with *CMT*, employing a *KUKA R1810* robot and a *Fronius TPS 400i* power source. To minimize specimen distortion during *WAAM*, the substrate was made of *Q235B* steel (analogous to rimmed low-carbon steel *St3*), selected for its lower cost. The potential influence of the substrate on the deposited metal's structure and properties is governed primarily by differences in thermal conductivity λ and, to a lesser extent, specific heat capacity C [17]. While the specific heat capacities are nearly identical (C_{Q235B} = 498 J/(kg·K), $C_{ER321(AISI\ 321)}$ = 494 J/(kg·K)), there is a significant difference in thermal conductivity (λ_{Q235B} = 54 W/(m·ºC), $\lambda_{ER321(AISI\ 321)}$ = 18 W/(m·ºC) at 200°C. This difference significantly affects heat transfer only for the initial 2–3 deposited layers. Afterwards, this difference dissapeared due to the high temperature and thickness of deposited layers that served as a heat barrier, thus making insufficient thermal conductivity of the substrate with increasing distance from it [10, 18]. This aligns with standard *WAAM* practice, where a substrate of common, low-cost steel like rimmed low-carbon steel *St3* is typically used. The substrate thickness was 10 mm to ensure sufficient strength and prevent deformation during the printing process.

A shielding gas mixture of 98% *Ar* and 2 % CO_2 was used. The feedstock was 1.2 mm diameter *ER321* austenitic stainless steel welding wire. The same grade was used for the rolled specimen to ensure scientific consistency and comparability of the obtained data. The chemical compositions of the wire, substrate, and rolled specimen are provided in Table 1.

Table 2 summarizes *WAAM + CMT* process parameters, and Fig. 1 presents a photograph and a process chart of the *WAAM + CMT* system.

The specimens were etched in a mixture of 67 wt.% HNO_3 and 33 wt.% *HCl*, and their microstructure was examined using an *Axio Observer A1m* inverted microscope (*Carl Zeiss*, Germany). The ferrite

Table 1

Chemical composition of the wire, substrate, and rolled product

Materials	Elemental composition, wt.%									
	C	*Si*	*Mn*	*P*	*S*	*Cr*	*Ni*	*Mo*	*Cu*	*Ti*
Wire	0.06	0.49	1.52	0.021	0.002	18.9	9.08	0.08	0.13	0.17
Substrate	0.18	0.16	0.45	0.019	0.019					
Rolled product	0.08	0.45	1.51	0,023	0.002	18.2	9.12	0.05		0.16

Table 2

***WAAM* + *CMT* process parameters**

Wire feed speed, m/min	4.5	Shielding gas rate, L/min	20
Printing speed, m/min	0.6	Voltage, V	19.1
Temperature, °C	200	Current, A	121

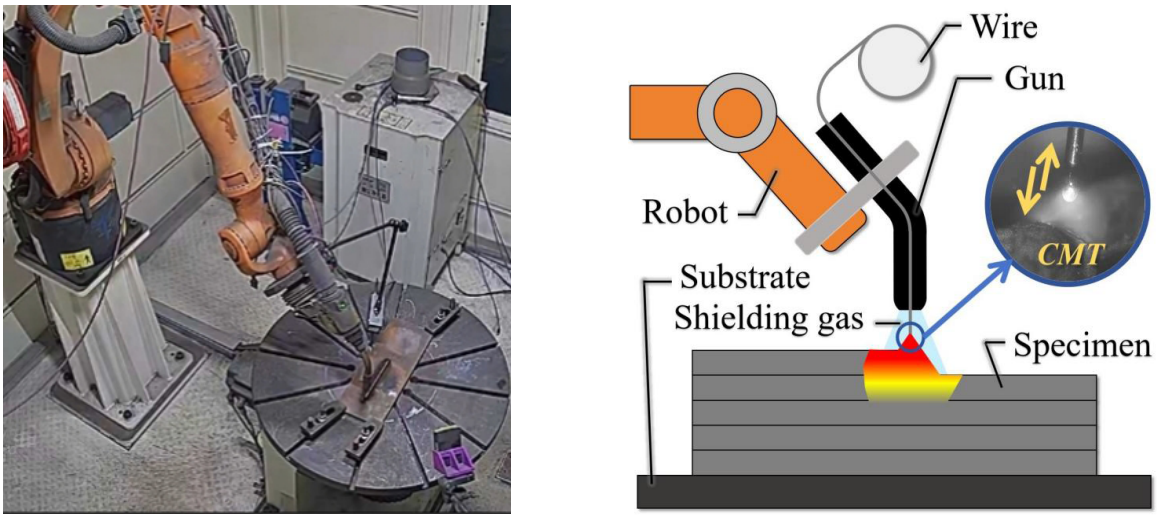

a *b*

Fig. 1. WAAM + CMT system:
full view (*a*), process chart (*b*)

content was determined from micrographs using the *ImageJ* image analysis software. Scanning electron microscopy with energy-dispersive X-ray spectroscopy (*SEM/EDS*) was performed on different regions of the *WAAM*-fabricated specimen using a *Quanta 200 3D SEM* (*FEI Company*, USA) equipped with an energy-dispersive X-ray analyzer.

The schematic in Fig. 2, *b* illustrates the specimen sections and their orientation. The *OX* axis is aligned with the scanning direction, the *OY* axis is aligned with the transverse direction, and the *OZ* axis is aligned with the layer-building direction (normal to the deposition plane). Microhardness was measured using a *DuraScan-10* hardness tester (*EMCO TEST*, Austria) with a 0.1 kgf load and a 10 s dwell time.

Tensile tests were performed at room temperature on an *MIM 4* testing machine at a crosshead speed of 2 mm/min. The dimensions of the 2 mm thick dog-bone specimens are shown in Fig. 2, *c*. Although milling involves high-strain-rate deformation, stress-strain curves obtained at room temperature provide relevant insight into the material's mechanical properties [19]; therefore, high-temperature tensile testing was not conducted in this study.

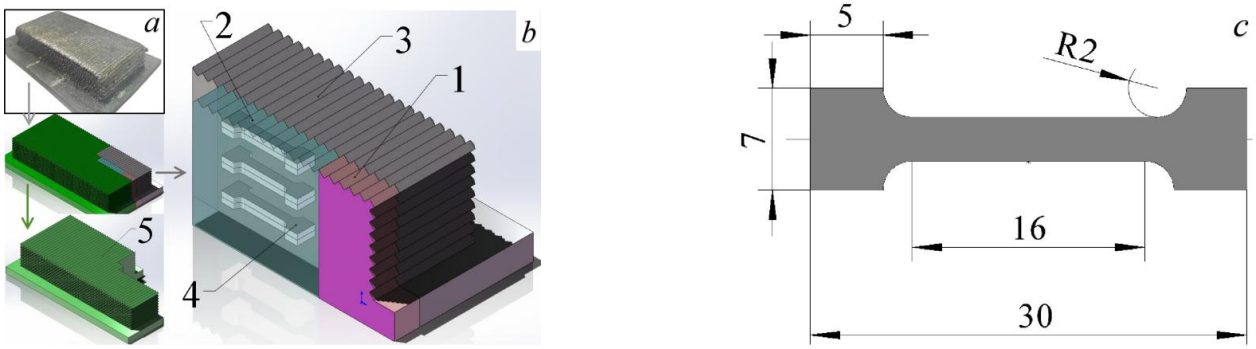

Fig. 2. Photograph of the *WAAM*-fabricated specimen (*a*), samples cut from the specimen (*b*), dimensions of 2 mm thick dog bone specimens, mm (*c*):

1 – for metallographic analysis, 2 – for tensile strength testing, 3 – for milling, 4 – dog bone specimens, 5 – for other analyses

The locations for metallographic observation, tensile test specimen selection, and hardness measurements were in the lower part of the *WAAM*-fabricated specimen (approximately 3 mm from the substrate) and in the upper part (approximately 3 mm from the top surface).

The specimen was milled on a *Concept Mill 155 CNC* milling machine (*EMCO*, Austria). A photograph of the milling setup is shown in Fig. 3, *a*. As illustrated in Fig. 3, *b*, a *Kistler 9257BA* (Switzerland) three-component dynamometer (**1**) was used to measure the three components of the milling force: the feed force $\boldsymbol{Fx} = \boldsymbol{Ph}$, acting along the feed direction $\boldsymbol{s_m}$; lateral force $\boldsymbol{Fy} = \boldsymbol{Pv}$, acting normal to the $\boldsymbol{s_m}$ direction; axial force $\boldsymbol{Fz} = \boldsymbol{Px}$, acting along the cutter axis. In the *Kistler 9257BA* software, the directions of the ***Fx***, ***Fy*** and ***Fz*** axes were aligned with the direction of forces acting during the axial turn process. Within the measured range, the dynamometer's sensitivity was 7.5 N, with a measurement error of ±0.005%.

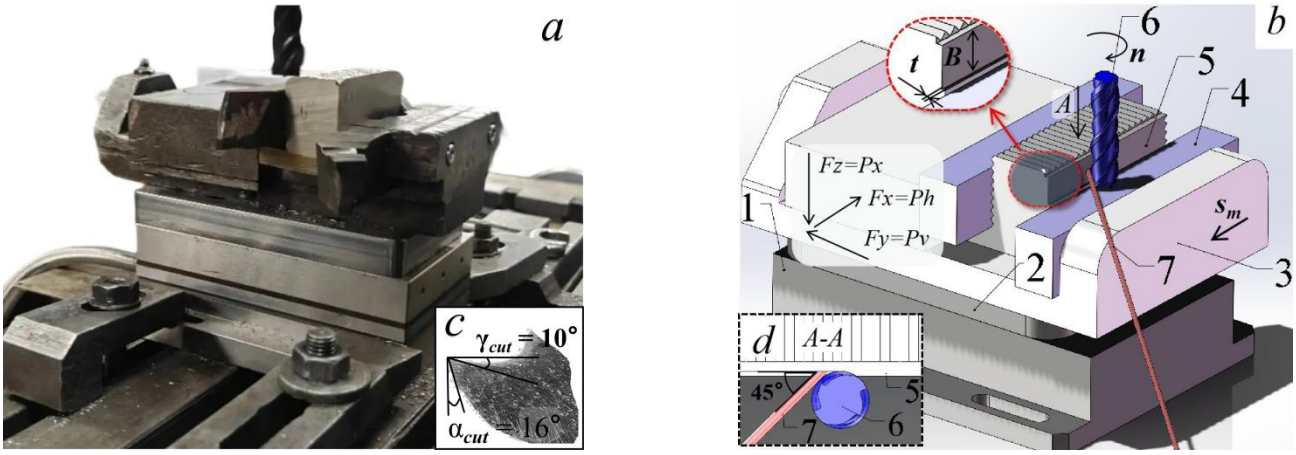

Fig. 3. Photograph (*a*), three-dimensional model (*b*) of dynamometer, cutter, specimen, cutter tooth geometry installed in the main section plane (*c*), and position of the infrared thermometer beam, specimen and cutter along ***A*** arrow. ***B*** – milling width, ***t*** – milling depth, ***n*** – rotational speed of a cutter, $\boldsymbol{s_m}$ – feed per minute (*d*)

A mounting plate (**2**) is used to secure the machine vice (**3**) to the dynamometer (**1**). A fixture (*4*), attached to the vice jaw (**3**), features a shallow longitudinal groove into which the specimen is inserted to prevent displacement of the 80×35×34 mm *WAAM*-fabricated or rolled specimen (**5**) relative to the vice jaws. The rolling direction of the specimen was aligned parallel to the feed direction $\boldsymbol{s_m}$.

The end mill (**6**), with a 12 mm diameter, four teeth, and a 35° lead angle, was made of *VK10* hard alloy coated with an *AlTiN* layer applied by physical vapor deposition (*PVD*). The tool's face angle ($\boldsymbol{\gamma_{cut}}$) and back angle ($\boldsymbol{\alpha_{cut}}$) are indicated in Fig. 3, *c*. The infrared beam path (**7**) from a *YCR-D2080AR* single-beam *IR* thermometer (*Wuxi Youtian Environmental Technology*, China) was oriented tangentially to the cutter,

forming a 45° angle with the machined surface (Fig. 3, *d*). The temperature measurement point ***T*** was set at the average height of the machined surface. The thermometer's emissivity was set to 0.39.

Surface roughness *Ra* was measured using a *TR200* profilometer (*JITA*, China) at the average height of the vertical machined surface (i.e., at the center of the milling width ***B***). A *GP-304K* microscope (*KSGAOPIN*, China) was used to examine the machined surface. The reported values for the ***Ph***, ***Pv*** and ***Px*** forces, the cutting temperature ***T***, and the surface roughness *Ra* represent the average of three measurements.

The milling parameters are given in Table 3. These parameters, commonly used for conventional (non-CNC) milling machines, were selected to ensure practical relevance. In this work, conventional (up) milling was employed, a technique often used for machining rough surfaces with uneven topography, such as those typical of *WAAM*-fabricated specimens after deposition. The cutter overhang was maintained at 35 mm.

Table 3

Milling parameters

Parameters	Feed per minute s_m, mm/min	Rotational speed ***n***, rpm	Milling width ***B***, mm	Milling depth ***t***, mm
Values	25, 50, 80, 125, 160, 200	315	7	1

Results and Discussion

The chemical composition of different regions in the *WAAM*-fabricated specimen is presented in Table 4. The carbon content in both the upper and lower regions is comparable to that of the initial wire. A slightly higher carbon content in the lower region is attributed to carbon diffusion from the substrate into the first (lower) deposited layer. The diffusion of iron (*Fe*), present in high concentration in the substrate, into the deposited layer also reduces the *Cr* and *Ni* content in the lower region of the specimen.

Table 4

X-ray microanalysis results for different regions of *WAAM*-fabricated specimen

Regions	Chemical composition, wt.%						
	Cr	*Ni*	*C*	*Si*	*Mn*	*Fe*	Other elements
Lower	17.86	8.02	0.18	0.31	1.3	70.21	2.12
Central	18.75	9.18	0.05	0.51	1.61	68.33	1.57
Upper	18.97	9.12	0.06	0.53	1.62	68.14	1.56

Based on the elemental composition of the austenitic stainless steel, Eqs. (1) and (2) [22] can be used to calculate the chromium (Cr_{eq}) and nickel (Ni_{eq}) equivalents, and Eq. (3) is used to determine the solidification mechanism in different regions of the *WAAM*-fabricated specimen. The different solidification mechanisms result in a different sequence of γ-ferrite and δ-austenite formation:

$$Cr_{eq} = \text{wt.\% } Cr + \text{wt.\% } Mo + 1.5 \times \text{wt.\% } Si + 0.5 \times \text{wt.\% } Nb \quad (1)$$

$$Ni_{eq} = \text{wt.\% } Ni + 0.5 \times \text{wt.\% } Mn + 30 \times \text{wt.\% } C + 30 \times \text{wt.\% } N \quad (2)$$

Order *A* ($Cr_{eq}/Ni_{eq} < 1.25$): $L \rightarrow (L + \gamma) \rightarrow \gamma$,

Order *AF* ($1.25 < Cr_{eq}/Ni_{eq} < 1.48$): $L \rightarrow (L + \gamma) \rightarrow (L + \gamma + \delta) \rightarrow (\gamma + \delta)$,

Order *FA* ($1.48 < Cr_{eq}/Ni_{eq} < 1.95$): $L \rightarrow (L + \delta) \rightarrow (L + \delta + \gamma) \rightarrow (\delta + \gamma)$,

$$\text{Order } F\ (Cr_{eq}/Ni_{eq} > 1.95)\text{: } L \rightarrow (L + \delta) \rightarrow \delta \quad (3)$$

where Cr_{eq}/Ni_{eq} is the ratio of chromium to nickel equivalents.

Although Eq. (3) does not account for the cooling rate effect, it provides a reliable approximation [23]. The calculated Cr_{eq}/Ni_{eq} ratios for different regions of the *WAAM*-fabricated specimen are presented in Table 5.

Table 5

Cr_{eq}/Ni_{eq} ratio for different parts of *WAAM*-fabricated specimen

Regions	Cr_{eq}	Ni_{eq}	Cr_{eq}/Ni_{eq} ratio
Lower	18.32	14.07	1.30
Middle	19.51	11.49	1.70
Upper	19.77	11.73	1.69

The low *Ti* content was omitted from the calculations due to its negligible influence on the solidification mechanism. As shown in Table 5 and Eq. (2), solidification in the upper and central regions corresponds to order *AF*, while in the lower region it corresponds to order *FA*. This shift in solidification order in the lower region is caused by carbon diffusion from the substrate into the deposited layer, which stabilizes austenite.

The microstructure of the lower region of the *WAAM*-fabricated specimen is shown in Fig. 4, *a*. Vermicular ferrite is observed, which is typical for solidification order *AF* [22]. The initial ferrite content is low. Furthermore, carbon diffusion within the deposited layer is limited during the eutectic reaction due to the high cooling rate inherent to the deposition process, which is particularly rapid near the substrate. This further suppresses ferrite formation and reduces its content. Carbon atoms diffusing from the substrate into the deposited layer increase the carbon content in the lower region, thereby enhancing its hardness.

As seen in Fig. 4, *b*, the central region of the *WAAM*-fabricated specimen consists of ferrite with a dendritic morphology. Multiple thermal cycles in this region promote elemental diffusion that favors ferrite formation, resulting in increased ferrite thickness and the highest ferrite content [23].

Fig. 4, *c* shows the microstructure of the upper region. The limited number of thermal cycles provides insufficient diffusion of ferrite-promoting elements, leading to the formation of fine ferrite precipitates. Nevertheless, the overall ferrite content remains high. The fine and closely spaced ferrite impedes dislocation slip at phase interfaces, enhancing the hardness of this region. Concurrently, the limited thermal cycling results in insufficient remelting in the upper region, generating numerous pores that reduce hardness but increase ultimate elongation.

At the specimen periphery (Fig. 4, *d*), the microstructure is similar to that of the upper region. Both the ferrite content and hardness are comparable to the upper region and remain high. This microstructure is primarily attributed to a higher cooling rate. Furthermore, the peripheral area with distinct microstructural properties was of insufficient size to cut off standard-sized tensile specimens. Therefore, tensile testing was not performed on the peripheral material.

For the rolled specimen (Fig. 4, *e*), the ferrite is finer and its content is lower compared to the *WAAM*-fabricated specimen. The ferrite morphology is elongated along the rolling direction. The hardness of the rolled specimen is similar to that of the upper region and periphery of the *WAAM*-fabricated specimen. However, both the hardness and ultimate elongation of the rolled specimen are higher.

As shown in Table 6 and Fig. 5, the microstructure and mechanical properties of regions within the *WAAM*-fabricated specimen – excluding the lower region – exhibit certain variations. These variations are comparable to data reported for wire-feed electron beam additive manufacturing [10]. However, the differences are minor and do not significantly affect milling machinability. Consequently, the milling machinability of different specimen regions was not investigated separately. The lower region of the

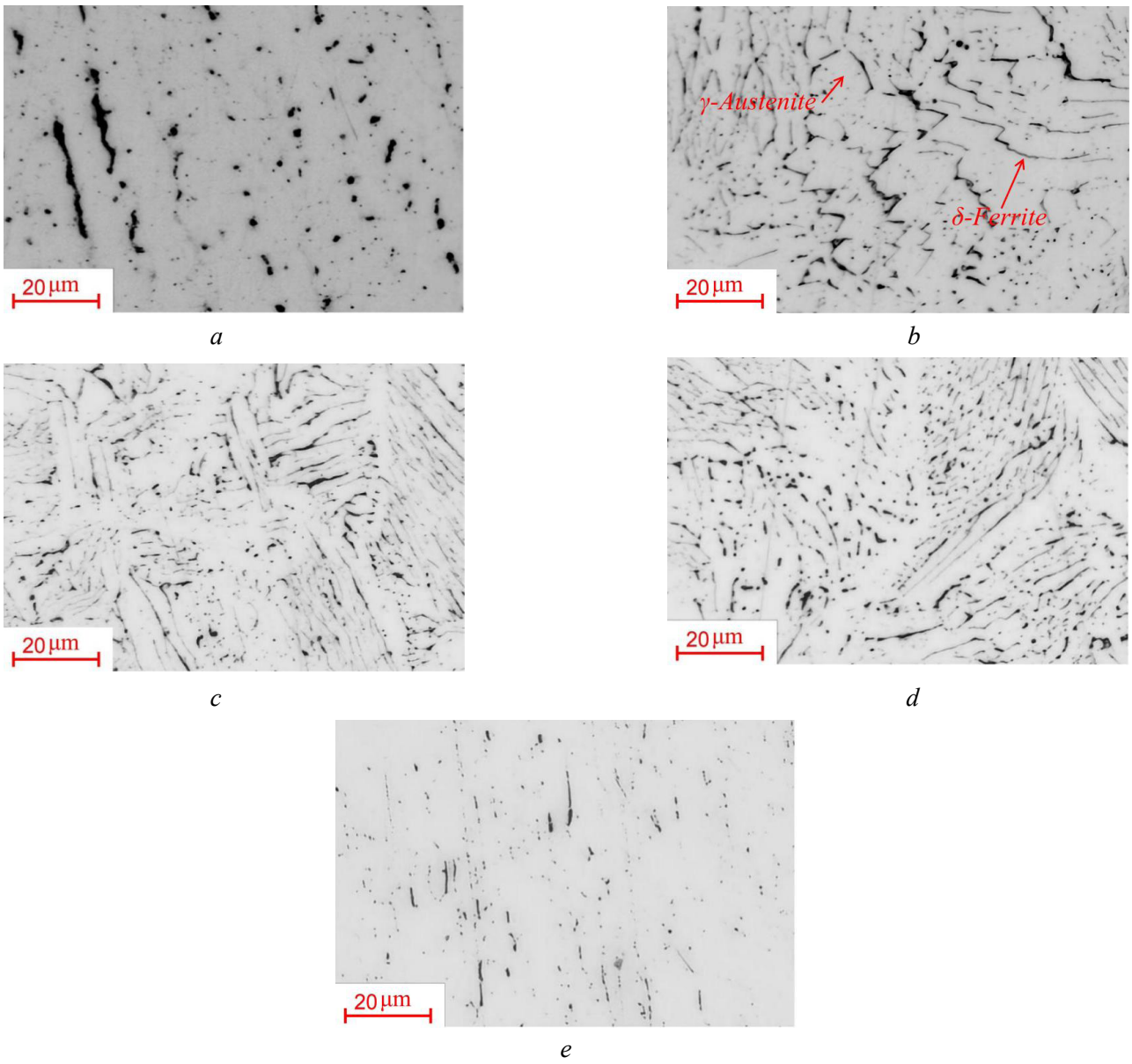

Fig. 4. Microstructure at lower (*a*), central (*b*), upper (*c*) and periphery (*d*) parts of *WAAM*-fabricated specimen and rolled specimen (*e*)

Table 6

Hardness and ferrite content in *WAAM*-fabricated and rolled specimens

	WAAM-fabricated				Rolled
	Lower region	Central region	Upper region	Peripheral region	
Hardness $HV_{0.1}$	226.7 ± 4.6	227.6 ± 5.3	231.4 ± 9.2	230.1 ± 4.1	230 ± 3.1
Ferrite content φ_{δ}, %	5.8 ± 1.4	17.56 ± 5.2	16.21 ± 4.8	15.89 ± 6.3	3.2 ± 1.2

specimen, along with the substrate, was removed by wire electrical discharge machining (*EDM*). As *EDM* falls outside the scope of this paper, the milling machinability of the lower region is not included in this study.

Fig. 6 shows the key parameters in a cross-sectional view of the cutter and workpiece (specimen) during conventional (up) milling. The values for $\boldsymbol{s_m}$, ***n***, ***Ph*** and ***Pv*** correspond to those defined in Fig. 3.

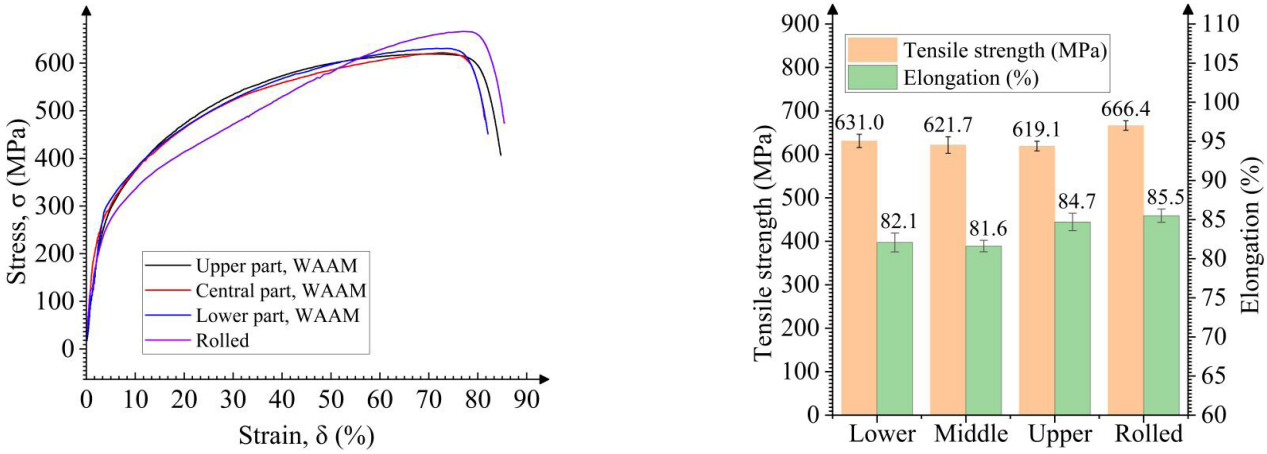

Fig. 5. Tensile stress-strain diagrams, ultimate tensile strength, and ultimate elongation of *WAAM*-fabricated and rolled specimens

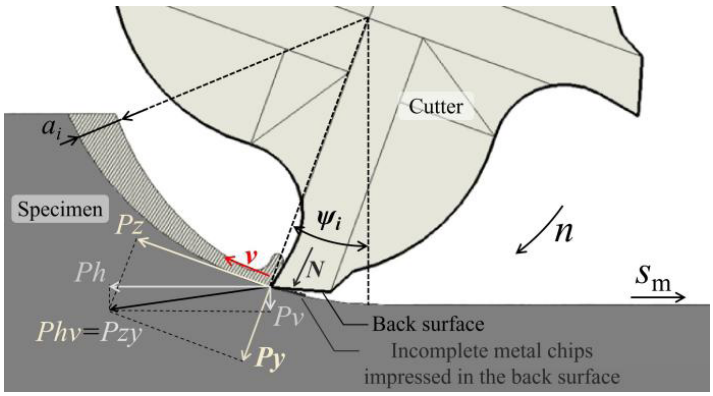

Fig. 6. Direction of forces ***Ph***, ***Pv***, ***Pz***, and ***Py*** in conventional milling

The engagement angle (ψ) indicates the angular position of the cutter tooth tip relative to its point of entry into the workpiece (specimen). The cutting speed is denoted by v, and the instantaneous thickness of cut by a_i. The tangential force (P_z) acts along the direction of the cutting speed, while the radial force (P_y) acts perpendicular to the cutter axis. P_z and P_y are derived from Eqs. (4) and (5) with minor simplification based on geometrical relations. The normal force (N), acting on the tool back surface, arises from the interference of uncut material with this surface and is a component of the radial force P_y.

$$P_z = P_h \times \cos\psi - P_v \times \sin\psi \tag{4}$$

$$P_y = P_h \times \sin\psi + P_v \times \cos\psi \tag{5}$$

The cutting speed v, thickness of cut a_i, tangential force P_z, and radial force P_y vary with the engagement angle ψ. The resultant force P_{hv} is derived from P_h and P_v, while P_{zy} is derived from P_z and P_y. These resultant forces are calculated as:

$$P_{hv} = \sqrt{\left(P_h^2 + P_v^2\right)}, \tag{6}$$

$$P_{zy} = \sqrt{\left(P_z^2 + P_y^2\right)}. \tag{7}$$

The total cutting force P_{tot} is calculated from:

$$P_{tot} = \sqrt{\left(P_h^2 + P_v^2 + P_x^2\right)}. \quad (8)$$

Fig. 7 shows the variation of these parameters with feed rate s_m. The feed per tooth s_t is obtained from:

$$s_t = s_m / (n \times z). \quad (9)$$

where $z = 4$ is the number of cutter teeth.

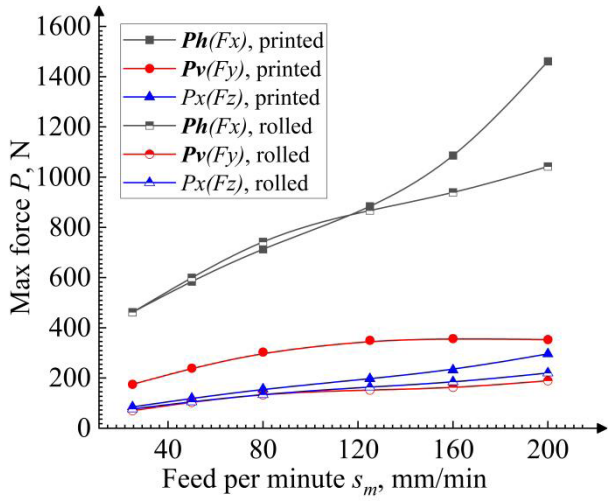

a

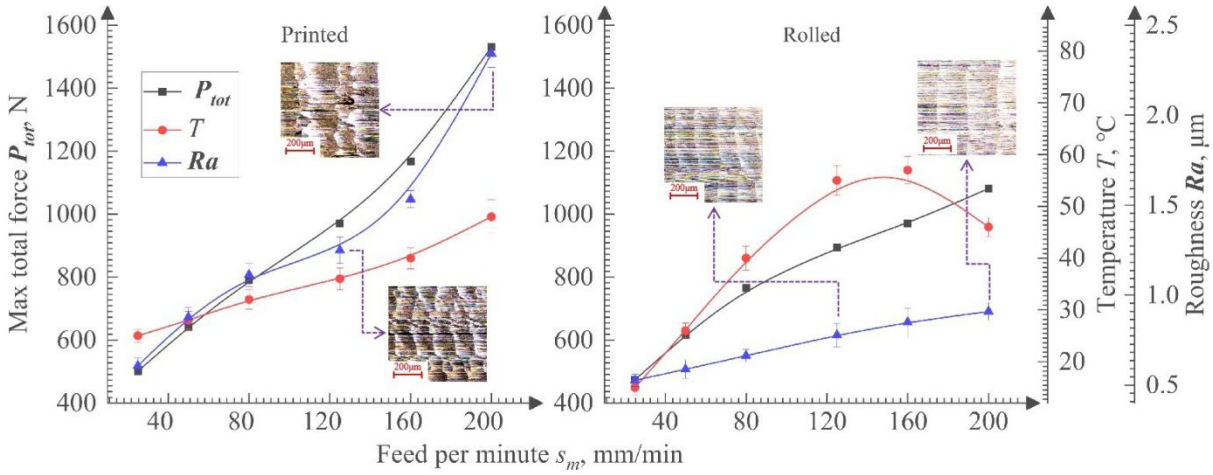

b

Fig. 7. Dependences of the feed rate s_m on the feed force ***Ph***, lateral force ***Pv*** and axial force *Px* (*a*) and maximum resultant force P_{tot}, temperature ***T***, and surface roughness ***Ra*** (*b*) during milling of fabricated and rolled specimens

Fig. 7, *a* shows the dependence of the feed force components P_h, P_v, and P_x on the feed rate s_m during milling of the *WAAM*-fabricated and rolled specimens. All force components increase with s_m due to the greater thickness of cut a_t. The feed force P_h is the largest and most sensitive to changes in s_m. This behavior is attributed to the use of conventional milling in this experiment, combined with a low depth of cut ***t*** (only 8.3% of the cutter diameter). In conventional milling, when the cutter tooth engages the workpiece, the resultant force P_{zy} acts primarily in the feed direction. The low depth of cut prevents significant changes in the direction of P_{zy} before the tooth exits the cut. Consequently, P_{zy} has the greatest influence on the feed force P_h [24], making P_h the largest and most sensitive component to variations in s_m. As a result, the total force P_{tot} follows a trend similar to P_h, albeit slightly exceeding it (Fig. 7, *b*).

The lateral force P_v is lower for the rolled specimen than for the *WAAM*-fabricated one. This is because less material is displaced beneath the cutting edge due to the higher tensile strength of the rolled material (see Fig. 5, *b*). This phenomenon is examined in greater detail in [25]. The cutting edge radius of a fresh tool ranges from 1 to 5 μm, depending on the hard alloy grain size and the face and back angles [26].

At high s_m values, the growth of P_h with further increases in s_m slows during milling of the rolled specimen, whereas this effect is not observed for the *WAAM*-fabricated specimen. The differences in P_v and P_h between the two materials can be explained by their distinct properties (Table 6, Fig. 5) and the effect of s_m on cutting temperature T (Fig. 7, *a*).

The lower hardness of the *WAAM*-fabricated specimen allows more material to be displaced beneath the rounded cutting edge. In the cutting and indentation zone, this material undergoes work hardening due to plastic deformation, increasing its yield strength. During elastic recovery of the machined surface, this hardened material contacts the tool back surface, generating a high normal force N and, consequently, a higher passive force P_v (Fig. 6) [27]. These two factors account for the elevated P_v during milling of the *WAAM*-fabricated specimen.

At low s_m, the cut thickness a_i is also small, promoting greater material displacement beneath the cutting edge and, as noted, leading to increased P_v and temperature.

At high s_m, the increased cut thickness facilitates material removal over the back surface and reduces indentation beneath the cutting edge, lowering the temperature. The significantly lower ductility of the *WAAM*-fabricated specimen also promotes chip fracture and removal, reducing the radial force on the face surface. This diminishes the elastic strain in the primary deformation zone and the subsequent elastic recovery against the back surface. According to *Das* and *Ghosh* [28], reduced contact lengths on both the face surface and back surface enhance heat dissipation and lower cutting temperatures. The absence of a slowdown in the increase of P_h at higher feed rates is due to the larger volume of material removed and the lower temperatures [13].

As shown in Fig. 8, *b*, surface roughness increases with feed rate (s_m). This relationship is explained in Figs. 8, *a* and 8, *b*: the higher feed per tooth (s_t) resulting from an increased s_m (see Eq. 9) leads to a greater height of the residual material protrusion (h_p, red areas in Fig. 8, *a*, *b*), which consequently increases surface roughness. Furthermore, surface roughness is higher for the *WAAM*-fabricated specimen than for the rolled specimen, with the difference becoming significant at higher s_m values. This difference is attributed to the lower hardness but higher yield strength of the *WAAM*-fabricated specimen, meaning it offers greater resistance to plastic deformation. Fig. 8, *c* shows the machined surface of the *WAAM*-fabricated specimen.

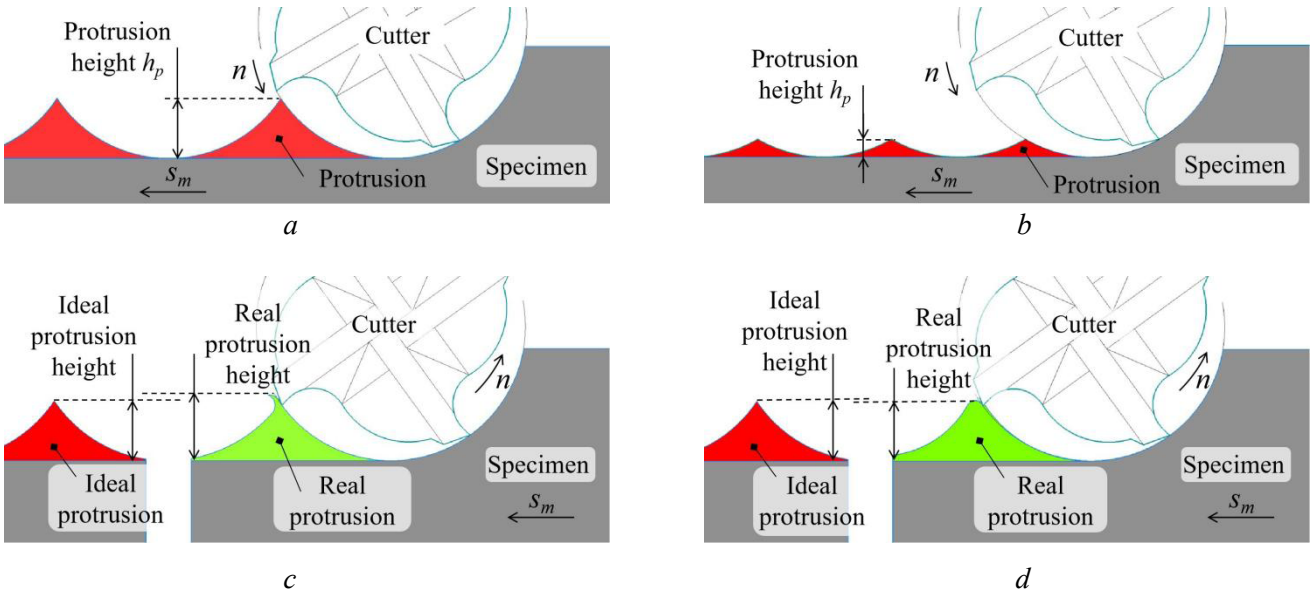

Fig. 8. Profiles of the machined surface at low (*a*) and high (*b*) feed per minute s_m and machined surface during opposing milling of *WAAM*-deposited (*c*) and rolled (*d*) specimens

The upper region of the protrusion is forced against the tool back surface due to the material's low hardness, undergoing severe plastic deformation. The lower region deforms less due to the higher yield strength. Consequently, in milling the *WAAM*-fabricated specimen, the protrusion height (h_p) is greater, resulting in higher surface roughness.

Conversely, the rolled specimen has higher hardness and lower yield strength, offering less resistance to plastic deformation. Its machined surface is shown in Fig. 8, *e*. The protrusion deforms more readily due to the lower yield strength, while less material is displaced beneath the tool back surface due to the higher hardness. Thus, in milling the rolled specimen, the protrusion height is smaller, leading to lower surface roughness.

The difference in protrusion height between the two materials becomes more pronounced with increasing feed rate, which correspondingly amplifies the difference in their surface roughness.

Conclusion

1. The lower region of the *WAAM*-fabricated *ER321* austenitic stainless steel specimen solidified according to order *FA*, influenced by the *Q235B* steel substrate.

2. A vermicular ferrite microstructure was observed in the lower region, while dendritic ferrite characterized the central and upper regions. The hardness (~230 HV0.1) was similar in all regions and comparable to that of the rolled specimen.

3. The ultimate tensile strength was below 631 MPa in all regions of the *WAAM*-fabricated specimen, compared to 666 MPa for the rolled specimen.

4. At low feed rates, the feed force was similar for both specimens. However, as the feed rate increased, the feed force became lower for the rolled specimen than for the *WAAM*-fabricated specimen due to thermal effects.

5. During milling, the surface roughness of the *WAAM*-fabricated specimen was higher than that of the rolled specimen, due to the former's combination of higher yield strength and lower hardness. This difference became more significant at higher feed rates, reaching approximately 1 μm.

References

1. Ahuja B., Karg M., Schmidt M. Additive manufacturing in production: Challenges and opportunities. *Proceedings of SPIE*, 2015, vol. 9353, pp. 11–20. DOI: 10.1117/12.2082521.

2. Altaf K., Abdul Rani A.M., Raghavan V.R. Prototype production and experimental analysis for circular and profiled conformal cooling channels in aluminium filled epoxy injection mould tools. *Rapid Prototyping Journal*, 2013, vol. 19 (4), pp. 220–229. DOI: 10.1108/13552541311323236.

3. Rozvany G.I. A critical review of established methods of structural topology optimization. *Structural and Multidisciplinary Optimization*, 2009, vol. 37, pp. 217–237. DOI: 10.1007/s00158-007-0217-0.

4. Sobczak J.J., Drenchev L. Metallic functionally graded materials: A specific class of advanced composites. *Journal of Materials Science & Technology*, 2013, vol. 29 (4), pp. 297–316. DOI: 10.1016/j.jmst.2013.02.006.

5. Klimenov V.A., Kolubaev E.A., Han Z, Chumaevskii A.V., Dvilis E.S., Strelkova I.L., Drobyaz E.A., Yaremenko O.B., Kuranov A.E. Modul' uprugosti i tverdost' titanovogo splava, sformirovavshegosya v usloviyakh elektronnogo luchevogo splavleniya pri EB-pechati provolokoi [Modulus of elasticity and hardness of titanium alloy formed under conditions of electron beam melting in EB wire printing]. *Obrabotka metallov (tekhnologiya, oborudovanie, instrumenty) = Metal Working and Material Science*, 2023, vol. 25, no. 4, pp. 180–201. DOI: 10.17212/1994-6309-2023-25.4-180-201.

6. Chen J., Wei H., Zhang X., Peng Y., Kong J., Wang K. Flow behavior and microstructure evolution during dynamic deformation of 316 L stainless steel fabricated by wire and arc additive manufacturing. *Materials & Design*, 2021, vol. 198, p. 109325. DOI: 10.1016/j.matdes.2020.109325.

7. Long P., Wen D., Min J., Zheng Z., Li J., Liu Y. Microstructure evolution and mechanical properties of a wire-arc additive manufactured austenitic stainless steel: Effect of processing parameter. *Materials*, 2021, vol. 14 (7), p. 1681. DOI: 10.3390/ma14071681.

8. Prakash K.S., Kannan A.R., Pramod R., Kumar N.P., Shanmugam N.S. Microstructure, mechanical properties and fracture toughness of SS 321 stainless steel manufactured using wire arc additive manufacturing. *Transactions of the Indian Institute of Metals*, 2023, vol. 76 (2), pp. 537–544. DOI: 10.1007/s12666-022-02713-3.

9. Chinakhov D.A., Akimov K.O. Formation of the structure and properties of deposited multilayer specimens from austenitic steel under various heat removal conditions. *Metals*, 2022, vol. 12 (9), p. 1527. DOI: 10.3390/met12091527.

10. Astafurova E.G., Panchenko M.Y., Moskvina V.A., Maier G.G., Astafurov S.V., Melnikov E.V., Kolubaev E.A. Microstructure and grain growth inhomogeneity in austenitic steel produced by wire-feed electron beam melting: The effect of post-building solid-solution treatment. *Journal of Materials Science*, 2020, vol. 55 (22), pp. 9211–9224. DOI: 10.1007/s10853-020-04424-w.

11. Khodabakhshi F., Farshidianfar M.H., Gerlich A.P., Nosko M., Trembošová V., Khajepour A. Effects of laser additive manufacturing on microstructure and crystallographic texture of austenitic and martensitic stainless steels. *Additive Manufacturing*, 2020, vol. 31, p. 100915. DOI: 10.1016/j.addma.2019.100915.

12. Thompson M.K., Moroni G., Vaneker T., Fadel G., Campbell R.I., Gibson I., Martina F. Design for additive manufacturing: Trends, opportunities, considerations, and constraints. *CIRP Annals*, 2016, vol. 65 (2), pp. 737–760. DOI: 10.1016/j.cirp.2016.05.004.

13. Babaev A.S., Kozlov V.N., Semenov A.R., Shevchuk A.S., Ovcharenko V.A., Sudarev E.A. Issledovanie sil rezaniya i obrabatyvaemosti pri frezerovanii poroshkovoi korrozionno-stoikoi stali, poluchennoi po tekhnologii pryamogo lazernogo vyrashchivaniya [Investigation of cutting forces and machinability during milling of corrosion-resistant powder steel produced by laser metal deposition]. *Obrabotka metallov (tekhnologiya, oborudovanie, instrumenty) = Metal Working and Material Science*, 2024, vol. 26, no. 2, pp. 38–56. DOI: 10.17212/1994-6309-2024-26.2-38-56.

14. Dabwan A., Anwar S., Al-Samhan A.M., AlFaify A., Nasr M.M. Investigations on the effect of layers' thickness and orientations in the machining of additively manufactured stainless steel 316L. *Materials*, 2021, vol. 14 (7), p. 1797. DOI: 10.3390/ma14071797.

15. Guo P., Zou B., Huang C., Gao H. Study on microstructure, mechanical properties and machinability of efficiently additive manufactured AISI 316L stainless steel by high-power direct laser deposition. *Journal of Materials Processing Technology*, 2017, vol. 240, pp. 12–22. DOI: 10.1016/j.jmatprotec.2016.09.005.

16. Milton S., Duchosal A., Chalon F., Leroy R., Morandeau A. Thermal study during milling of Ti6Al4V produced by Electron Beam Melting (EBM) process. *Journal of Manufacturing Processes*, 2019, vol. 38, pp. 256–265. DOI: 10.1016/j.jmapro.2018.12.027.

17. Kok Y., Tan X.P., Wang P., Nai M.L.S., Loh N.H., Liu E., Tor S.B. Anisotropy and heterogeneity of microstructure and mechanical properties in metal additive manufacturing: A critical review. *Materials & Design*, 2018, vol. 139, pp. 565–586. DOI: 10.1016/j.matdes.2017.11.021.

18. *Marochnik stali i splavov* [Database of Steels and Alloys]. Website, 2003–2025. Available at: https://www.splav-kharkov.com (accessed 17.10.2025).

19. Chen J., Wei H., Zhang X., Peng Y., Kong J., Wang K. Flow behavior and microstructure evolution during dynamic deformation of 316 L stainless steel fabricated by wire and arc additive manufacturing. *Materials & Design*, 2021, vol. 198, p. 109325. DOI: 10.1016/j.matdes.2020.109325.

20. Astafurov S., Astafurova E. Phase composition of austenitic stainless steels in additive manufacturing: A review. *Metals*, 2021, vol. 11 (7), p. 1052. DOI: 10.3390/met11071052.

21. Bajaj P., Hariharan A., Kini A., Kürnsteiner P., Raabe D., Jägle E.A. Steels in additive manufacturing: A review of their microstructure and properties. *Materials Science and Engineering: A*, 2020, vol. 772, p. 138633. DOI: 10.1016/j.msea.2019.138633.

22. Elmer J.W., Allen S.M., Eagar T.W. Microstructural development during solidification of stainless steel alloys. *Metallurgical Transactions A*, 1989, vol. 20, pp. 2117–2131. DOI: 10.1007/BF02650298.

23. Zheng B., Zhou Y., Smugeresky J.E., Schoenung J.M., Lavernia E.J. Thermal behavior and microstructural evolution during laser deposition with laser-engineered net shaping: Part I. Numerical calculations. *Metallurgical and Materials Transactions A*, 2008, vol. 39, pp. 2228–2236. DOI: 10.1007/s11661-008-9557-7.

24. Martyushev N.V., Kozlov V.N., Qi M., Tynchenko V.S., Kononenko R.V., Konyukhov V.Y., Valuev D.V. Production of workpieces from martensitic stainless steel using electron-beam surfacing and investigation of cutting forces when milling workpieces. *Materials*, 2023, vol. 16 (13), p. 4529. DOI: 10.3390/ma16134529.

25. Zhang Q., She L., Guo T., Kozlov V.N. [Calculation of stresses in the cutting tool at the beginning of cutting]. *Nauchnaya initsiativa inostrannykh studentov i aspirantov* [Scientific initiative of foreign students and postgraduates]. Collection of reports of the III International scientific and practical conference, Tomsk, 2023, pp. 450–456. (In Russian).

26. Kozlov V.N., Babaev A.S., Shults N.A., Semenov A.S., Shevchuk A.S. Study of a methodology for calculating contact stresses during blade processing of structural steel. *Metals*, 2023, vol. 13 (12), p. 2009. DOI: 10.3390/met13122009.

27. Gusarov A.V., Yadroitsev I., Bertrand P., Smurov I. Heat transfer modelling and stability analysis of selective laser melting. *Applied Surface Science*, 2007, vol. 254 (4), pp. 975–979. DOI: 10.1016/j.apsusc.2007.08.074.

28. Das C.R., Ghosh A. Performance of carbide end mills coated with new generation nano-composite TiAlSiN in machining of austenitic stainless steel under near-dry (MQL) and flood cooling conditions. *Journal of Manufacturing Processes*, 2023, vol. 104, pp. 418–442. DOI: 10.1016/j.jmapro.2023.09.020.

Conflicts of Interest

The authors declare no conflict of interest.